Assessment of mechanically induced changes in helical fiber microstructure using diffusion tensor imaging

Roberto Pineda Guzman[a], Noel M. Naughton[b], Shreyan Majumdar[b], Bruce Damon[c], Mariana E. Kersh[a,b,d,*]

[a]*Department of Mechanical Science & Engineering, University of Illinois Urbana-Champaign*
[b]*Beckman Institute of Advanced Science & Technology; University of Illinois Urbana-Champaign*
[c]*Carle Foundation Hospital, Urbana, Illinois*
[d]*Carle Illinois College of Medicine; University of Illinois Urbana-Champaign*

Abstract

Non-invasive methods to detect microstructural changes in collagen-based fibrous tissues are necessary to differentiate healthy from damaged tissues *in vivo* but are sparse. Diffusion Tensor Imaging (DTI) is a non-invasive imaging technique used to quantitatively infer tissue microstructure with previous work primarily centered in neuroimaging applications. Yet, it is still unclear how DTI metrics relate to fiber microstructure and function in musculoskeletal tissues such as ligament and tendon in part because of the high heterogeneity inherent to such tissues. To address this limitation, we assessed the ability of DTI to detect microstructural changes caused by mechanical loading in tissue-mimicking helical fiber constructs of known structure. Using high-resolution optical imaging, we found that static and fatigue loading resulted in decreased sample diameter and a re-alignment of the macro-scale fiber twist angle similar with the direction of loading. However, the DTI measurements suggest microstructural differences in the effect of static versus fatigue loading that were not apparent at the bulk level. Specifically, static load resulted in an increase in diffusion anisotropy and a decrease in radial diffusivity suggesting radially-uniform fiber compaction. In contrast, fatigue loads resulted in increased diffusivity in all directions and a change in the alignment of the principal diffusion direction away from the constructs' main axis suggesting fiber compaction and microstructural disruptions in fiber architecture. These results provide quantitative evidence of the ability of DTI to detect mechanically-induced changes in tissue microstructure that is not apparent at the bulk level, thus confirming it's potential as a non-invasive measure of microstructure in helically architected collagen-based tissues such as ligament and tendon.

Keywords: fiber, microstructure, mechanics, fatigue, diffusion MRI

1. Introduction

Over one third of all musculoskeletal injuries in the United States involve connective tissue deterioration, resulting in an annual incidence of more than 10 million injuries [1]. To detect damage accumulation and improve the detection and treatment of connective

*Corresponding author
Email address: mkersh@illinois.edu (Mariana E. Kersh)

tissue injuries, it is necessary to quantify the underlying determinants that differentiate healthy from damaged soft tissues. Damage accumulation from repetitive loading manifests as changes in tissue microstructure [2]; however, most methods used to quantify connective soft tissue microstructure involve microscopic imaging [2, 3, 4, 5] which requires excision of tissue for examination.

Diffusion Tensor Imaging (DTI) is a non-invasive Magnetic Resonance Imaging (MRI) technique that measures the diffusion properties of water in tissues [6]. DTI is sensitive to physical barriers that restrict the movement of water molecules, providing a proxy measure of tissue microstructure. For example, the DTI metric radial diffusivity measures the degree to which water molecules are free to move in the direction perpendicular to the principal orientation of physical barriers in a material. Assuming the physical barriers mediating diffusion are transversely isotropic, radial diffusivity provides an indicator of the compaction of the physical barriers (e.g. collagen fibers, cells, or other constituents of the tissue) that would impede diffusion: tightly packed aligned fibers result in low radial diffusivity and high axial diffusivity. DTI metrics have been used to research brain neuronal structure[7], and in smaller scope, skeletal muscle [8, 9, 10]. Efforts to study connective collagen-rich tissues (breast, cartilage, artery, and cervix) are sparse, but have related DTI metrics to microstructure [11, 12, 13, 14, 15, 16], and biomechanical function [17].

DTI has been used to quantitatively assess pathologies and clinical interventions in ligaments and tendons [18, 19, 20, 21, 22, 23, 24, 25, 26]. However, these studies are limited to correlations between DTI metrics and injury states and lack information on the biomechanical causation of these relationships. To our knowledge, only one study has related DTI metrics to tissue composition in tendon [27] but did not relate DTI metrics to microstructural assessments. A clear understanding of the relationship between collagen fiber microstructure, mechanical behavior, and DTI metrics is needed but is challenging because of the heterogeneous nature of ligaments and tendons [28] and the multifactorial contribution of cellullar and non-collagenous extracellullar components to the DTI metrics measured in biological materials [29].

To circumvent this challenge, tissue-mimicking materials with known fiber architecture can be used as microstructural phantoms and provide a platform to probe the sensitivity of DTI measurements to detect changes in fiber microstructure[30]. Anisotropic fiber phantoms have been used to model brain white matter, demonstrating that diffusion anisotropy increases with increased fiber density [31, 32] and that principal diffusion directions follow the principal orientation of the tissue fiber structure [33, 34]. *In silico* models of articular cartilage fiber networks have been used to study the effect of fiber density, orientation, and organization on diffusion properties [35]. However, hierarchical, helical fiber structures, such as those found in ligament and tendon [36, 37], have yet to be assessed with DTI.

Similar to ligament and tendon, engineered helical fiber constructs transfer loads through interfibrillar shear between discontinuous fibers [38, 39, 40], and lose volume in response to uniaxial tensile loading [41, 42]. Previously, we demonstrated that helically architected fiber constructs mimic the hierarchical microstructure and tensile behavior of ligaments [43]. These fiber constructs have also been used to replicate the shear behavior of tendon and ligament [44]. Additionally, the constructs' fiber diameters (10-20 μm) and fiber separation distances (10-40 μm) are at the same length scale of collagen fibers in tendon and ligament [45].

Using tissue-mimicking fiber constructs as microstructural DTI phantoms, the aim

of this study was to establish relationships between fiber microstructure, mechanical function and DTI metrics. We quantified the changes in structure and DTI metrics caused by mechanical loading on the tissue-mimicking fibers. These relationships will provide the necessary framework for future studies to interpret mechanically-induced changes in DTI metrics in biological ligaments, tendons, and other transversely isotropic and helically architected collagen-based tissues.

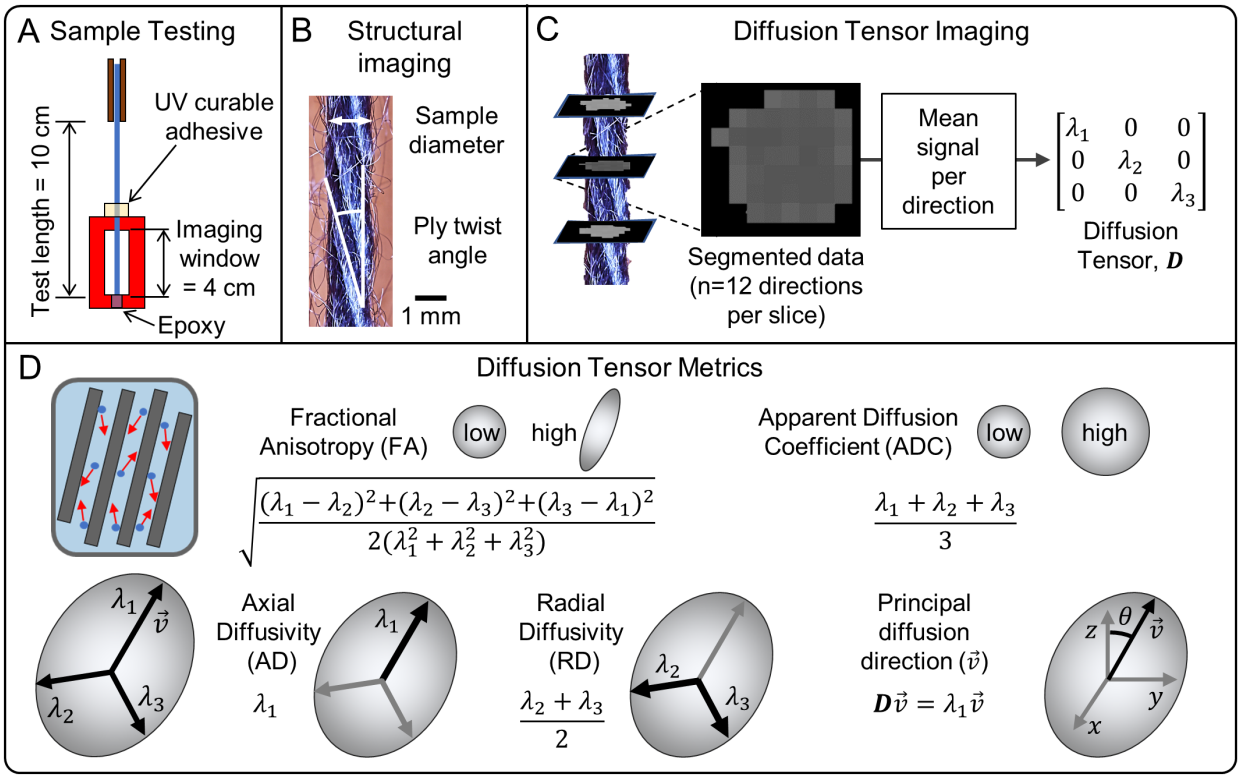

Figure 1: Outline of experimental methodology. A) Mechanical loading protocols applied to the tissue-mimicking phantom samples. B) Structural parameters measured on the phantoms: Phanton diameter and ply twist angle. C) Diffusion Tensor Imaging data obtained from phantoms submerged in distilled water. D) DTI metrics used to analyze the changes in fiber microstructure caused by the mechanical loading protocols.

2. Materials and Methods

2.1. Sample preparation

Fifteen helically architected tissue-mimicking samples (Caron, linear density = 590 tex) were used for this study. The samples were randomly assigned to three groups (n=5/group): control, static load, and fatigue load. A custom MRI compatible fixture, with a 4 cm optical imaging window, was used to secure and image the samples (Figure 1A). One end of the sample was attached to the fixture using water-resistant epoxy (J-B MarineWeld). All samples were fixed after mechanical loading and imaged at their respective loading configuration.

2.2. Mechanical loading protocols

An exposed test length of 10 cm was used for all samples. The samples were subjected to 50 preconditioning axial loading cycles (2 – 25 N, 1.15 Hz) prior to mechanical loading.

Unloaded controls: The control group was loaded to 0.2 N using a uniaxial testing system (Instron model 5967, Instron, USA) to standardize the initial length of the samples and then fixed in place. The samples were then attached to the fixture using an ultraviolet (UV) curable adhesive (Bluffix PW).

Static load: The free end of the static sample group was clamped using pneumatic grips. The samples were loaded to 5 N and then attached to the fixture using the UV curable adhesive. Static load data were collected at 100 Hz.

Fatigue load: The samples assigned to the fatigue group were subjected to 10,000 loading cycles using a uniaxial dynamic mechanical system (ElectroForce 3200, TA Instruments, USA) using a sinusoidal waveform ramping between 2-25N at 5Hz. Ten loading cycles were needed for the dynamic testing system to achieve a steady state of the 2 - 25 N load limits. Displacement data were collected for all samples at the 2 and 25 N load points for each loading cycle and continuous mechanical data were collected for one sample at 500 Hz. Following fatigue loading, the sample was loaded to 0.2 N and then secured within the imaging fixture.

The maximum strain, $\epsilon_{max,n}$, during each fatigue cycle (n) was computed as:

$$\epsilon_{max,n} = \frac{u_{25N,n} - u_{2N,10}}{100mm} \times 100\% \tag{1}$$

where $u_{25N,n}$ was the displacement at 25N for cycle n, $u_{2N,10}$ was the displacement at 2N for the 10th cycle, and 100 mm was the original length of the sample.

The cyclic stiffness was computed as:

$$k_n = \frac{25N - 2N}{u_{25N,n} - u_{2N,n}} \tag{2}$$

where $u_{25N,n}$ and $u_{2N,10}$ were the displacement at 25 N and 2 N for cycle n, respectively. The difference between the maximum and minimum cyclic load was assumed to be 23 N per the fatigue protocol. All analyses were performed in Matlab (version R2018b).

2.3. Bulk scale structural imaging

All samples were imaged using a high-resolution camera (100 MP, PhaseOne, Denmark) to measure the sample diameter and ply twist angle, indices of the primary hierarchical structure, using custom Matlab (version R2018b) code and ImageJ. Sample diameter was measured by segmenting the sample from the background, binarizing the image, and calculating the mean distance between the sample edges. The ply twist angle of each sample was measured manually using ImageJ (Figure 1B).

2.4. Microstructural imaging

Micro-Computed Tomography (μCT) scans were acquired of one sample from each group to quantify fiber microstructure. The control and static load samples were scanned using an Xradia MicroXCT 400 (Zeiss, Germany) scanner (voltage = 25 kV, power = 5 W, resolution = 2.1 x 2.1 x 2.1 μm, FOV = 2.08 x 2.08 x 2.08 mm), while the fatigue sample was scanned using a Rigaku CT Lab HX130 (Rigaku,Japan) scanner (voltage = 50 kV, source power = 8 W, resolution = 2.5 x 2.5 x 2.5 μm, FOV = 2.36 x 2.12 x 2.47 mm). The fatigue sample was resized to have an in-plane resolution of 2.1 x 2.1μm.

The μCT data were binarized (Amira, Thermo Fisher Scientific, USA) and imported into Matlab (version R2018b). For each CT slice, the fiber density was quantified as the

ratio between the total fiber pixel area and the area of the smallest polygon enclosing all the fibers. The second moment of area of the sample's fiber cross section with respect to the cross section's minor axis was computed to evaluate fiber dispersion.

2.5. Diffusion Tensor Imaging

Finally, DTI data were collected on all samples. The diffusion encoding parameters used for the DTI sequences were optimized through numerical simulations of the Bloch-Torrey equation [46] using a binarized cross-section of the sample's fibers that were acquired in a previous study using μCT [43]. A parameter sweep of gradient strengths and diffusion times was performed to identify the parameter combinations that would maximize the encoding of structural information into the diffusion-weighted signal, under the constraint of adequate signal-to-noise ratio (SNR).

The samples were submerged in distilled water and a vacuum chamber was used to remove air bubbles. The submerged samples were then imaged using a 9.4 T MRI system (Bruker, MA, USA). DTI was performed using an echo-planar imaging sequence (TE/TR = 180/4200 ms, 12 directions, 12 excitations, b = 600 s/mm^2, diffusion gradient duration δ = 80 ms, and diffusion gradient separation Δ = 86 ms). Twenty slices were acquired per sample (slice thickness = 375 µm, in-plane resolution = 150 x 150 µm, field of view = 19.2 x 19.2 x 7.5 mm). T2-weighted images were also acquired to visualize the sample geometry using a Rapid Imaging with Refocused Echoes (RARE) sequence (TE/TR = 10/4300 ms, slice thickness = 375 µm, in-plane resolution = 150 x 150 µm, field of view = 19.2 x 19.2 x 7.5 mm). The T2-weighted images were used to segment the sample's region of interest (ROI) from the surrounding water by segmenting all voxels with at least a 15% decrease in the fibers T2-weighted signal relative to the signal measured in voxels corresponding to water.

All volumes acquired from the T2 and DTI scans were manually registered. SNR maps of the DTI images were computed using the dwidenoise function available in MRtrix3.0 [47, 48]. To reduce the bias caused by noise when computing the diffusion tensor, the individual diffusion directional signals in the sample's ROI were averaged in each slice of the DTI scans resulting in an average SNR$>$20 in the non-diffusion weighted images. The diffusion tensor of each slice was computed using the average non-diffusion weighted and diffusion weighted signals of each slice with the *signal2tensor2* function of the publicly available DTI muscle toolbox [49] (Figure 1C). The tensor was diagonalized to calculate the principal eigenvalues (λ_1, λ_2, and λ_3). The eigenvalues were used to calculate the following DTI metrics:

Fractional Anisotropy (FA) was calculated as:

$$FA = \sqrt{\frac{(\lambda_1 - \lambda_2)^2 + (\lambda_2 - \lambda_3)^2 + (\lambda_3 - \lambda_1)^2}{2(\lambda_1^2 + \lambda_2^2 + \lambda_3^2)}} \tag{3}$$

Apparent Diffusion Coefficient (ADC) was calculated as:

$$ADC = \frac{\lambda_1 + \lambda_2 + \lambda_3}{3} \tag{4}$$

Radial Diffusivity (RD) was calculated as the mean of the 2nd and 3rd eigenvalues. Axial Diffusivity (AD) is equivalent to the first eigenvalue and the principal diffusion direction ($\vec{v}$) indicates the direction of maximum diffusion (λ_1) calculated from the diffusion tensor $\mathbf{D}$. The Z-orientation angle, θ, between the sample's main axis and the principal diffusion direction was also computed. A structural interpretation of each

MRI metric is shown in (Figure 1D). All MRI data-processing steps, except for the noise computations, were conducted in Matlab (version R2018b).

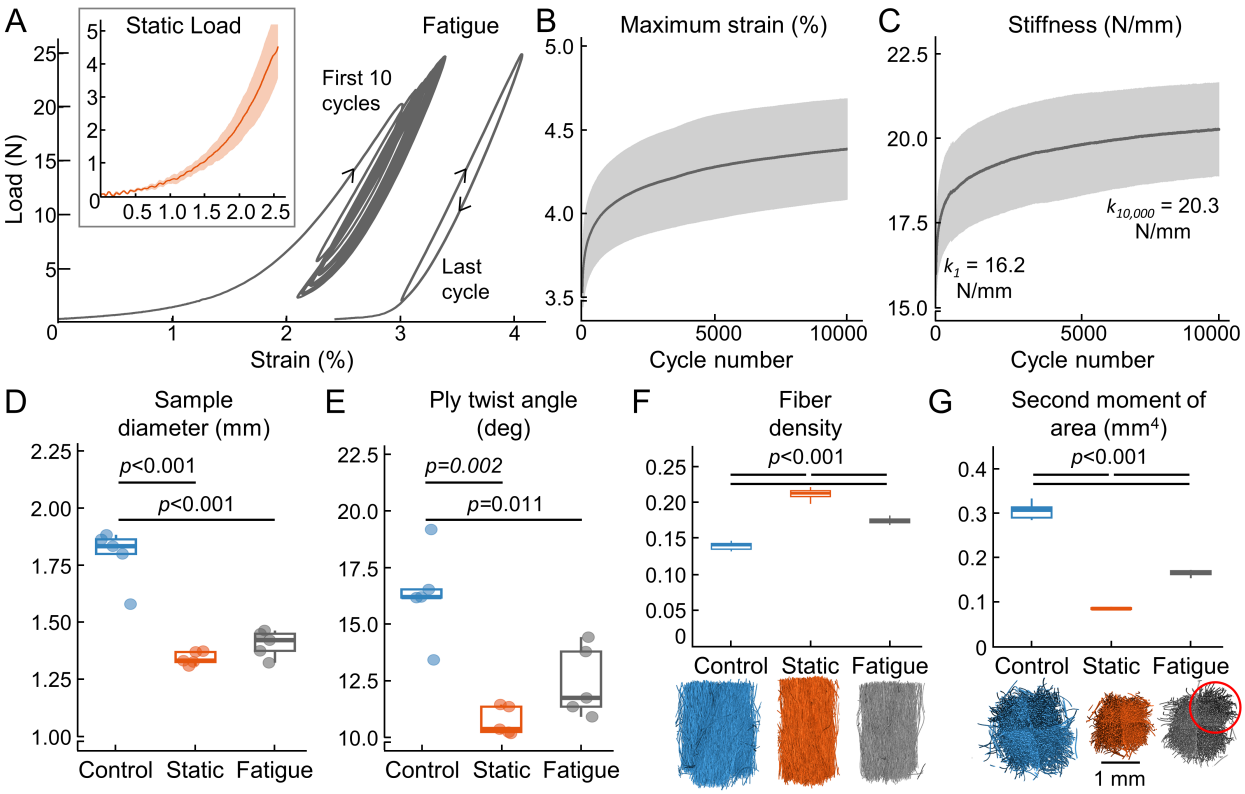

Figure 2: A) Load-strain curves obtained from the static load and fatigue samples. B-C) Maximum strain, $\epsilon_{max,n}$, and stiffness, k_n, as a function of loading cycle on the fatigued samples. D-E) Changes in sample diameter and ply twist angle between the control, static load, and fatigue sample groups. F-G) Changes in fiber density and second moment of area of the sample's cross section. The red circle highlights the observed fiber disruptions in the fatigued sample.

2.6. Statistical analysis

Normality of all measurements was tested using a Shapiro-Wilks test. All structural property measurements were normally distributed, thus unpaired t-tests were used to evaluate the differences in the structural parameters between the sample groups (α = 0.05). Differences between the distributions of microstructural parameters and DTI metrics of the static load and fatigued group with respect to the control group were evaluated using Kolmogorov-Smirnov tests (α = 0.05). All statistical analyses were conducted in R (version 4.2.3).

3. Results

3.1. Effect of loading on mechanical and structural properties

Static loading: Static loading resulted in a J-shaped load-strain curve reflecting a bulk scale mechanical response characteristic of collagen-rich tissues (Figure 2A). To reach the 5 N load, the samples were displaced 2.69 $\pm$ 0.23 mm (2.69 $\pm$ 0.23%

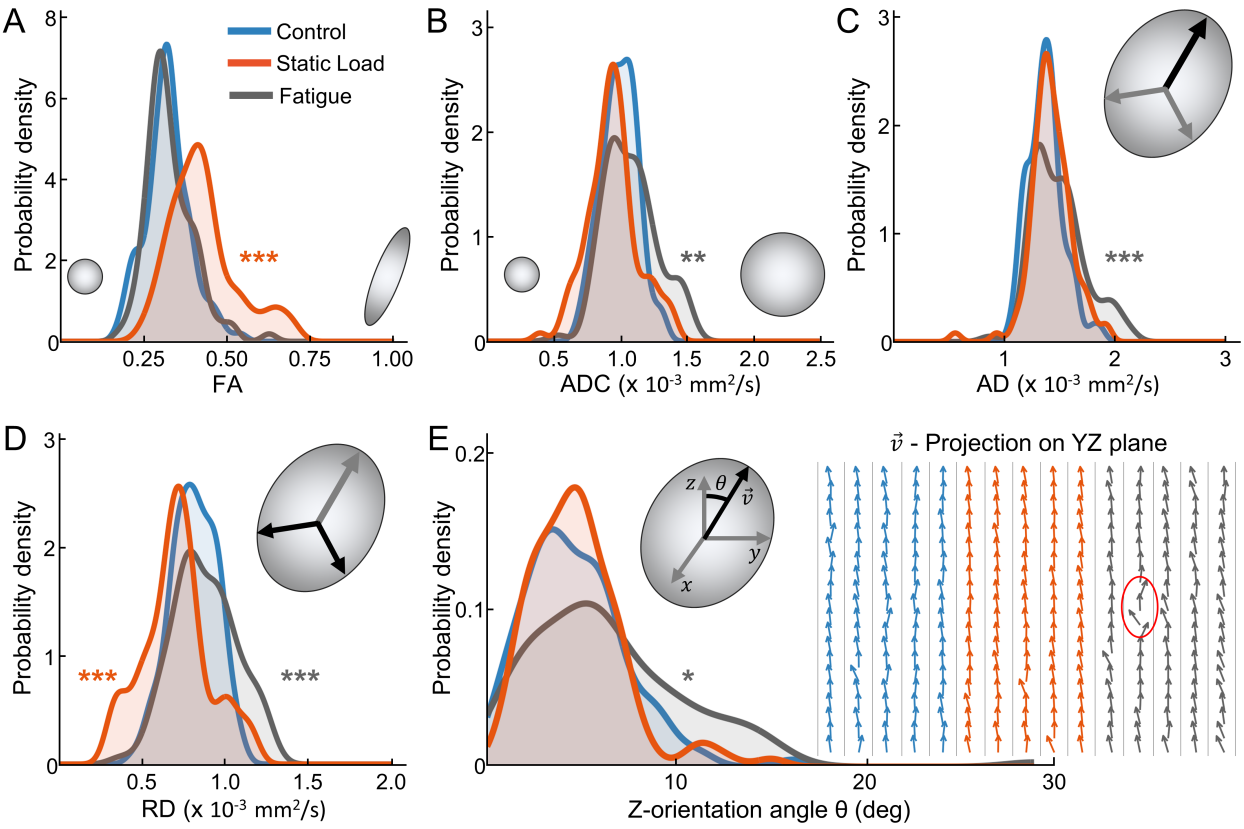

Figure 3: A-D) Probability density distributions of FA , ADC, AD and, RD in the control, static load, and fatigue groups. E) Probability density distribution of the Z-orientation angle in the three groups and visualized projection of the principal diffusion direction ($\vec{v}$). Each arrow represents the YZ projection of $\vec{v}$ computed on each slice and each column represents the twenty slices of each sample. Arrows circled in red highlight a local misalignment in $\vec{v}$. * p <0.05, ** p <0.01 & *** p <0.001 refer to comparisons with respect to the control group.

uniaxial strain). Static loading resulted in a 25.1% decrease in sample diameter from 1.79 $\pm$ 0.12 mm in the control samples to 1.34 $\pm$ 0.03 mm in the loaded samples (Figure 2D, $p < 0.001$). When compared to the control samples, the macroscopic ply twist angle decreased by 34.3% when subjected to static load, from a ply twist angle of 16.3 $\pm$ 2.04^o in the control group to a ply twist angle of 10.7 $\pm$ 0.63^o in the loaded group (Figure 2D, $p = 0.002$).

The microCT analyses revealed changes in sample microstructure. The fiber density was intially 0.14 $\pm$ 0.003 for the control sample and increased by 50% ($p < 0.001$) to 0.21 $\pm$ 0.004 when subjected to static loading (Figure 2F). The second moment of area was 0.307 $\pm$ 0.011 mm^4 for the control sample and decreased ($p < 0.001$) to 0.08 $\pm$ 0.0012 mm^4 under static load (Figure 2G), $p < 0.001$).

Fatigue loading: Similar to the static load case, the fatigue loading protocol resulted in a J-shaped load response. All samples reached the secondary phase of fatigue loading by 10,000 loading cycles, which is characterized by a steady increase in the maximum strain and stiffness followed by the rapid increase observed in the primary phase [50] (Figure 2A-C). Fatigue loading resulted in a 24.5 $\pm$ 4% increase in max cyclic displacement and a 24.1 $\pm$ 0.7% increase in cyclic stiffness.

The fatigue loading protocol resulted in measurable macrostructural changes compared to unloaded samples and were similar to the changes that occurred due to static

loading. Fatigue loading decreased the sample diameter by 21.9% when compared to the control group ($p < 0.001$). The mean ply twist angle of the fatigued group decreased by 23.7% ($p = 0.011$) with respect to the control group (Figure 2E).

Fatigue loading resulted in a 23.7% increase in median fiber density (0.174 $\pm$ 0.003 for fatigue, Figure 2F). The median second moment of area decreased to 0.165 $\pm$ 0.003 mm^4 following fatigue loading ($p < 0.001$, Figure 2G). Notably, we observed local regions of fiber disruption in the μCT data of fatigued samples that were not observed with static loading (Figure 2G).

3.2. Effect of loading on DTI metrics

Of the DTI metric data, the FA, ADC, and RD of the control samples, the ADC of the static load samples, and the RD of the fatigue samples were normally distributed. The remaining data sets were non-normally distributed. Thus, we describe the results of DTI measurements using medians and median absolute deviations.

Tensile static loading resulted in changes in fractional anisotropy (FA) and radial diffusivity (RD). FA increased by 28.1% ($p<0.001$), from 0.32 $\pm$ 0.04 in the control group to 0.41 $\pm$ 0.05 in the loaded group. RD decreased by 13.0% ($p<0.001$) with static loading when compared to the control group, from 0.81 $\pm$ 0.10x10^{-3} mm^2/s to 0.70 $\pm$ 0.10x10^{-3} mm^2/s. Static loading did not significantly change ADC, AD, and Z-orientation angle compared to the control samples (Figure 3).

Fatigue loading resulted in changes to the apparent diffusion coefficient (ADC), axial diffusivity (AD), radial diffusivity (RD), and the Z-orientation angle of the principal diffusion direction (θ). ADC increased 5.85% to 1.06 $\pm$ 0.13x10^{-3} mm^2/s ($p=0.003$), median AD increased 8.2% to 1.47 $\pm$ 0.16x10^{-3} mm^2/s ($p<0.001$), and median RD increased 4.94% to 0.85 $\pm$ 0.11x10^{-3} mm^2/s ($p=0.024$). The Z-orientation angle of the fatigued samples increased by 31.1% ($p=0.024$) compared to the control samples, with a z-orientation angle of 5.82 $\pm$ 2.80^o in the fatigued samples compared to 4.44^o in the control samples (Figure 3). These fatigue-induced changes were not homogeneous along the length of the sample; but instead were observed in specific locations along the samples' length (Figure 3E).

4. Discussion

This study identified DTI metrics related to mechanically-induced changes in tissue-mimicking phantoms. In the samples loaded under static tension, we found that increasing FA and decreasing RD were related to fiber compaction and increased fiber density (Figure 4). Previous studies have shown that FA is directly proportional to the fiber density of parallel fiber phantoms [31, 33]. While no data, to our knowledge, is available on how ADC, RD, and AD change as a function of fiber density in physical phantoms, *in silico* modeling of water diffusion in fiber networks shows that RD is more likely to be affected by an increase in fiber density than AD [35].

The decrease in sample diameter and ply twist angle and increase in fiber density of the static load group agrees with a mathematical formulation that accounts for fiber diametrical compaction as the main microstructural mechanism driving the sample's low-stress tensile behavior [42]. This formulation takes into account the compressibility of fiber-based materials derived from van Wyk's theory [51] and assumes negligible fiber sliding, interfibrillar friction, and fiber stretch during the toe region of the sample's load-displacement curve. Our results support the role of fiber diametrical compaction

as a potential mechanism that can explain the toe region and large Poisson's ratio [52] observed in ligaments and tendons with helically architected collagen fibrils and fibers. Coupled with the shear lag models [39], a more comprehensive microstructural description can be provided for the tensile behavior of ligaments and tendons.

In the fatigued samples, we found an increase in ADC, AD, and RD that suggests an increase in fiber disorganization, as more disorganized fiber structures would allow for more water diffusion. Increases in fiber disorganization could also account for the changes in principal diffusion direction and Z-orientation angle measured in the fatigued samples as disrupted fiber architecture could allow for more diffusion along the radial direction of the sample (Figure 4). Our microstructural data suggests that fatigued samples have local disruptions in fiber microstructure that account for these changes in DTI metrics (Figure 3E). The principal diffusion direction has been used as a surrogate for fiber orientation in both composite and biological fiber-based materials [53, 14, 11], thus our results suggest that fatigue loading results in microstructural disruptions that create axial misalignments in fiber microstructure.

Fatigued samples resulted in a biphasic fatigue behavior (Figure 2A-C) similar to tendons [54, 55] and fiber-based composites [56]. Although the microstructural mechanisms driving this behavior remain unknown, the fiber architecture of both tendon and fiber-based composites show a disruption in fiber architecture during the second phase of fatigue loading [54, 55, 2, 56]. Our results agree with these studies, as the DTI metrics and microCT data indicate a disruption in the fiber architecture in the fatigued group. Thus, DTI metrics may provide further insight into the microstructural changes in tissues that occur as a result of different pathologies.

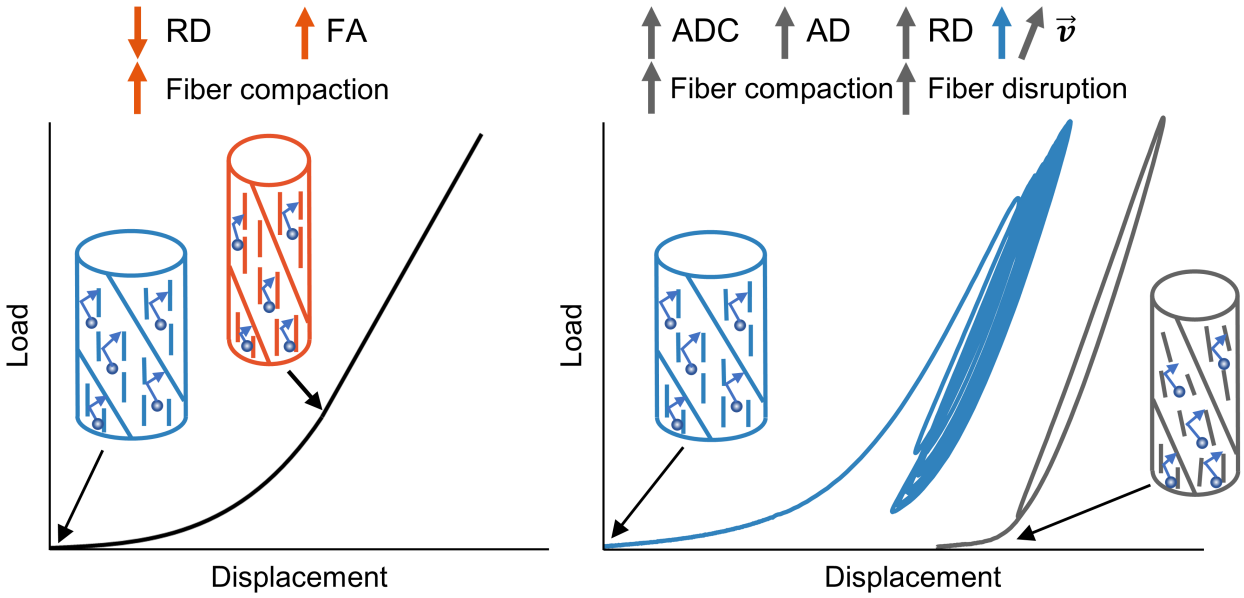

Figure 4: Schematic showing the changes in structure and DTI metrics caused by tensile and fatigue loading in tissue-mimicking phantoms.

In a previous study in the Achilles tendon, higher FA was correlated to lower collagen content and lower collagen alignment while higher ADC, AD, and RD were correlated to higher collagen content [27]. In breast cancer tissue, higher ADC was correlated to higher collagen content but FA was inversely correlated[11]. Thus, it is not clear whether tissue specific interpretations of DTI metrics and their relationship to the

tissue microenvironment are required to explain these contrasting findings with respect to FA. Nonetheless, DTI metrics have been correlated to clinical level findings.

In vivo studies of injured knee Anterior Cruciate Ligaments (ACLs) found a decrease in FA in those with higher levels of injury [23]. Anterior knee laxity is related to the mechanical integrity of the ACL [57] such that increased laxity (or ligament slack) in an injured knee indicates either structural or compositional degradation. After internal bracing, FA in the ACL has been reported to decrease and was hypothesized to be caused by an altered geometrical configuration of the tissue and was inversely correlated to knee laxity [22]. This is consistent with our results, as the application of tensile loading to remove the slack from our samples significantly increased their FA. Because the organization of cells in ligaments and tendons follows reorganization of collagen fibers due to their slackness [58], collagen fiber architecture could be an appropriate mediator of DTI metrics in this scenario. Both cellular and non-collagen extracellular components may also play a role in the DTI metrics of collagen-based tissues [29] and therefore a combination of both collagen fiber architecture and cellular content could explain these results. Notably, in the case of injury, swelling and inflammation may also contribute to changes in diffusion metrics.

Because our future goal is to assess the ability of DTI to measure the collagen fiber microstructure of tendons and ligaments, our phantoms provide a platform that allow us to only take into account changes in fiber architecture thus confirming the sensitivity of DTI to changes in microstructure. Previously, *in silico* and fiber based phantoms have been used to assess changes in cartilage [35] and white matter [31, 32, 33]. Since our phantoms are reproducible, have a tissue-mimicking well characterized microstructure, and induce diffusion-related changes, they are suitable for use as DTI phantoms [30] of helically architected fibers. To the best of our knowledge, this type of fiber architecture has not been studied before using DTI.

A limitation to this study is that we were not able to analyze the DTI metrics of our phantoms at the in-plane resolution in which the data was acquired. Because the phantoms are made of acrylic, the volume occupied by the phantom's fibers is MRI-invisible and decreases the overall signal acquired in each voxel. This led to some local areas of the samples having low SNR that could confound the DTI metrics we measured. This problem was solved by averaging the signals within the sample cross-section, however, at the expense of in-plane resolution. However, the variation along the samples' length was still quantified and differences were observed between the different sample groups. Another limitation is that our microstructural measurements were limited to one sample per group and are not co-registered to the DTI data we measured. We believe, nevertheless, that our μCT data are representative of the microstructural changes caused by mechanical loading in the three groups of samples. The frequency and extent of fiber disruptions that occurred due to fatigue, as well as the mechanisms that caused these disruptions, could be assessed in future studies.

Finally, the validity of these results in the complex environment of tendons, ligaments, and other biological tissues needs to be confirmed and is the subject of future work. We believe, however, that our results provide a framework to evaluate how DTI metrics are affected by changes to collagen fiber microstructure in ligaments and tendons. The ability of DTI to non-invasively detect microstructural changes within a macroscopic field of view support the use of DTI to non-invasively assess microstructural disruptions in biological and composite materials. Since current microscopic assessments in biological and composite materials are invasive and highly localized, DTI

could become an important tool to conduct damage analysis in fiber-based materials and more importantly ligaments, tendons, and other musculoskeletal soft tissues [59]. Thus, DTI metrics may serve as a biomarker for microstructural changes indicative of mechanical function of ligaments, tendons, and other collagen-rich tissues in order to detect damage prior to failure and monitor clinical interventions of ligaments and tendons in the clinical setting.

5. Conclusion

This work describes the ability of DTI to detect mechanically-induced changes in a tissue-mimicking microstructural phantom. We show that tensile loading results in increased fiber density caused by the diametrical compression of helically architected fibers and is associated with higher FA and lower RD. We also show that fatigue loading results in fiber architecture disruption that result in higher ADC, AD, and RD as well as a disruption in the alignment of the principal diffusion direction with the phantom's main axis. These results provide a framework to assess the ability of DTI to detect mechanically-induced changes in the collagen fiber microstructure of ligaments, tendons and other helically architected collagen-based soft tissues.

6. Acknowledgements

This project was funded by the Jump ARCHES endowment through the Health Care Engineering Systems Center and with support from the Biomedical Imaging Center of the Beckman Institute for Advanced Science and Technology at the University of Illinois Urbana-Champaign (UIUC-BI-BIC). We would like to acknowledge Tanya Josek and Josh Gibson from the Microscopy Suite of the Beckman Institute for obtaining the microCT images of the samples, Travis Ross from the Visualization Laboratory of the Beckman Institute for his technical assistance with the high-resolution camera systems, and David Ehrhardt from the Advanced Materials Testing and Evaluation Lab at the University of Illinois for the equipment and technical assistance needed to conduct the fatigue testing of the samples.

7. Conflict of Interest

Declarations of interest: none.

References

[1] United States Bone and Joint Initiative, The Burden of Musculoskeletal Diseases in the United States (BMUS), http://www.boneandjointburden.org (2014).

[2] S. E. Szczesny, C. Aeppli, A. David, R. L. Mauck, Fatigue loading of tendon results in collagen kinking and denaturation but does not change local tissue mechanics, Journal of Biomechanics 71 (2018) 251–256. doi:10.1016/j.jbiomech.2018.02.014.

[3] J. Chen, J. Kim, W. Shao, S. H. Schlecht, S. Y. Baek, A. K. Jones, T. Ahn, J. A. Ashton-Miller, M. M. Banaszak Holl, E. M. Wojtys, An Anterior Cruciate Ligament Failure Mechanism, American Journal of Sports Medicine 47 (9) (2019) 2067–2076. doi:10.1177/0363546519854450.

[4] J. Kim, S. Y. Baek, S. H. Schlecht, M. L. Beaulieu, L. Bussau, J. Chen, J. A. Ashton-Miller, E. M. Wojtys, M. M. Banaszak Holl, Anterior cruciate ligament microfatigue damage detected by collagen autofluorescence in situ, Journal of Experimental Orthopaedics 9 (1) (2022) 74. doi:10.1186/s40634-022-00507-6.

[5] N. W. Skelley, R. M. Castile, T. E. York, V. Gruev, S. P. Lake, R. H. Brophy, Differences in the microstructural properties of the anteromedial and posterolateral bundles of the anterior cruciate ligament, American Journal of Sports Medicine 43 (4) (2015) 928–936. doi:10.1177/0363546514566192.
[6] T. P. L. Roberts, E. S. Schwartz, Principles and implementation of diffusion-weighted and diffusion tensor imaging, Pediatric Radiology 37 (8) (2007) 739–748. doi:10.1007/s00247-007-0516-z.
[7] D. Le Bihan, H. Johansen-Berg, Diffusion MRI at 25: Exploring brain tissue structure and function, NeuroImage 61 (2) (2012) 324–341. doi:10.1016/j.neuroimage.2011.11.006.
[8] M. T. Hooijmans, B. M. Damon, M. Froeling, M. J. Versluis, J. Burakiewicz, J. J. G. M. Verschuuren, E. H. Niks, A. G. Webb, H. E. Kan, Evaluation of skeletal muscle DTI in patients with duchenne muscular dystrophy: SKELETAL MUSCLE DTI IN DMD, NMR in Biomedicine 28 (11) (2015) 1589–1597. doi:10.1002/nbm.3427.
[9] B. M. Damon, M. Froeling, A. K. W. Buck, J. Oudeman, Z. Ding, A. J. Nederveen, E. C. Bush, G. J. Strijkers, Skeletal muscle diffusion tensor-MRI fiber tracking: Rationale, data acquisition and analysis methods, applications and future directions: Skeletal Muscle Dt-Mri Fiber Tracking, NMR in Biomedicine 30 (3) (2017) e3563. doi:10.1002/nbm.3563.
[10] N. M. Naughton, J. G. Georgiadis, Global sensitivity analysis of skeletal muscle dMRI metrics: Effects of microstructural and pulse parameters, Magnetic Resonance in Medicine 83 (4) (2020) 1458–1470. doi:10.1002/mrm.28014.
[11] S. Kakkad, J. Zhang, A. Akhbardeh, D. Jacob, B. Krishnamachary, M. Solaiyappan, M. A. Jacobs, V. Raman, D. Leibfritz, K. Glunde, Z. M. Bhujwalla, Collagen fibers mediate MRI-detected water diffusion and anisotropy in breast cancers, Neoplasia (United States) 18 (10) (2016) 585–593. doi:10.1016/j.neo.2016.08.004.
[12] R. Meder, S. K. de Visser, J. C. Bowden, T. Bostrom, J. M. Pope, Diffusion tensor imaging of articular cartilage as a measure of tissue microstructure, Osteoarthritis and Cartilage 14 (9) (2006) 875–881. doi:10.1016/j.joca.2006.03.002.
[13] J. G. Raya, G. Melkus, S. Adam-Neumair, O. Dietrich, E. Mützel, B. Kahr, M. F. Reiser, P. M. Jakob, R. Putz, C. Glaser, Change of Diffusion Tensor Imaging Parameters in Articular Cartilage With Progressive Proteoglycan Extraction:, Investigative Radiology 46 (6) (2011) 401–409. doi:10.1097/RLI.0b013e3182145aa8.
[14] S. Ghazanfari, A. Driessen-Mol, G. J. Strijkers, F. M. Kanters, F. P. Baaijens, C. V. Bouten, A comparative analysis of the collagen architecture in the carotid artery: Second harmonic generation versus diffusion tensor imaging, Biochemical and Biophysical Research Communications 426 (1) (2012) 54–58. doi:10.1016/j.bbrc.2012.08.031.
[15] S. Ghazanfari, A. Driessen-Mol, G. J. Strijkers, F. P. T. Baaijens, C. V. C. Bouten, The Evolution of Collagen Fiber Orientation in Engineered Cardiovascular Tissues Visualized by Diffusion Tensor Imaging, PLOS ONE 10 (5) (2015) e0127847. doi:10.1371/journal.pone.0127847.
[16] W. Qi, P. Zhao, Z. Sun, X. Ma, H. Wang, W. Wu, Z. Wen, Z. Kisrieva-Ware, P. K. Woodard, Q. Wang, R. C. McKinstry, A. G. Cahill, Y. Wang, Magnetic resonance diffusion tensor imaging of cervical microstructure in normal early and late pregnancy in vivo, American Journal of Obstetrics and Gynecology 224 (1) (2021) 101.e1–101.e11. doi:10.1016/j.ajog.2020.07.014.
[17] U. Ferizi, I. Rossi, Y. Lee, M. Lendhey, J. Teplensky, O. D. Kennedy, T. Kirsch, J. Bencardino, J. G. Raya, Diffusion tensor imaging of articular cartilage at 3T correlates with histology and biomechanics in a mechanical injury model, Magnetic Resonance in Medicine 78 (1) (2017) 69–78. doi:10.1002/mrm.26336.
[18] X. Yang, M. Li, D. Chen, D. Shi, Z. Zhou, B. Zhu, Q. Jiang, Diffusion tensor imaging for anatomical and quantitative evaluation of the anterior cruciate ligament and ACL grafts: A preliminary study, Journal of Computer Assisted Tomography 38 (4) (2014) 489–494. doi:10.1097/RCT.0000000000000078.
[19] X. Yang, D. Chen, M. Li, D. Shi, B. Zhu, Q. Jiang, Diffusion tensor imaging of the anterior cruciate ligament graft after reconstruction: Repeatability and diffusion tensor imaging metrics, Journal of Computer Assisted Tomography 39 (2) (2015) 244–249. doi:10.1097/RCT.0000000000000198.
[20] P. Van Dyck, M. Froeling, E. De Smet, P. Pullens, M. Torfs, P. Verdonk, J. Sijbers, P. M. Parizel, B. Jeurissen, Diffusion tensor imaging of the anterior cruciate ligament graft, Journal of Magnetic Resonance Imaging 46 (5) (2017) 1423–1432. doi:10.1002/jmri.25666.
[21] P. Van Dyck, T. Billiet, D. Desbuquoit, P. Verdonk, C. H. Heusdens, E. Roelant, J. Sijbers, M. Froeling, Diffusion tensor imaging of the anterior cruciate ligament graft following reconstruction: A longitudinal study, European Radiology (2020). doi:10.1007/s00330-020-07051-w.

[22] P. Van Dyck, M. Froeling, C. H. Heusdens, J. Sijbers, A. Ribbens, T. Billiet, Diffusion tensor imaging of the anterior cruciate ligament following primary repair with internal bracing: A longitudinal study, Journal of Orthopaedic Research (December 2019) (2020) 1–13. doi:10.1002/jor.24684.
[23] S. Liu, J. Liu, W. Chen, L. Zhang, S. Wu, F. Wang, J. Pan, M. Luo, X. Liu, S. Zhang, Diffusion Tensor Imaging for Quantitative Assessment of Anterior Cruciate Ligament Injury Grades and Graft, Journal of Magnetic Resonance Imaging 52 (5) (2020) 1475–1484. doi:10.1002/jmri.27322.
[24] H. Sarman, H. Atmaca, O. Cakir, U. S. Muezzinoglu, Y. Anik, K. Memisoglu, T. Baran, C. Isik, Assessment of Postoperative Tendon Quality in Patients With Achilles Tendon Rupture Using Diffusion Tensor Imaging and Tendon Fiber Tracking, The Journal of Foot and Ankle Surgery 54 (5) (2015) 782–786. doi:10.1053/j.jfas.2014.12.025.
[25] K. Wengler, D. Tank, T. Fukuda, J. M. Paci, M. Huang, M. E. Schweitzer, X. He, Diffusion tensor imaging of human Achilles tendon by stimulated echo readout-segmented EPI (ste-RS-EPI): Wengler et al., Magnetic Resonance in Medicine 80 (6) (2018) 2464–2474. doi:10.1002/mrm.27220.
[26] K. Wengler, T. Fukuda, D. Tank, D. E. Komatsu, M. Paulus, M. Huang, E. S. Gould, M. E. Schweitzer, X. He, In vivo evaluation of human patellar tendon microstructure and microcirculation with diffusion MRI, Journal of Magnetic Resonance Imaging 51 (3) (2020) 780–790. doi:10.1002/jmri.26898.
[27] J. A. Zellers, M. Edalati, J. D. Eekhoff, R. McNish, S. Y. Tang, S. P. Lake, M. J. Mueller, M. K. Hastings, J. Zheng, Quantative MRI predicts tendon mechanical behavior, collagen composition, and organization, Journal of Orthopaedic Research (2022) jor.25471doi:10.1002/jor.25471.
[28] N. W. Skelley, R. M. Castile, P. C. Cannon, C. I. Weber, R. H. Brophy, S. P. Lake, Regional Variation in the Mechanical and Microstructural Properties of the Human Anterior Cruciate Ligament, American Journal of Sports Medicine 44 (11) (2016) 2892–2899. doi:10.1177/0363546516654480.
[29] B. Tornifoglio, A. J. Stone, R. D. Johnston, S. S. Shahid, C. Kerskens, C. Lally, Diffusion tensor imaging and arterial tissue: Establishing the influence of arterial tissue microstructure on fractional anisotropy, mean diffusivity and tractography, Scientific Reports 10 (1) (2020) 1–12. doi:10.1038/s41598-020-77675-x.
[30] E. Fieremans, H. H. Lee, Physical and numerical phantoms for the validation of brain microstructural MRI: A cookbook, NeuroImage 182 (June) (2018) 39–61. doi:10.1016/j.neuroimage.2018.06.046.
[31] E. Fieremans, Y. De Deene, S. Delputte, M. S. Özdemir, E. Achten, I. Lemahieu, The design of anisotropic diffusion phantoms for the validation of diffusion weighted magnetic resonance imaging, Physics in Medicine and Biology 53 (19) (2008) 5405–5419. doi:10.1088/0031-9155/53/19/009.
[32] E. Fieremans, Y. De Deene, S. Delputte, M. S. Özdemir, Y. D'Asseler, J. Vlassenbroeck, K. Deblaere, E. Achten, I. Lemahieu, Simulation and experimental verification of the diffusion in an anisotropic fiber phantom, Journal of Magnetic Resonance 190 (2) (2008) 189–199. doi:10.1016/j.jmr.2007.10.014.
[33] C. Poupon, B. Rieul, I. Kezele, M. Perrin, F. Poupon, J.-F. Mangin, New diffusion phantoms dedicated to the study and validation of high-angular-resolution diffusion imaging (HARDI) models: HARDI Validation Phantoms, Magnetic Resonance in Medicine 60 (6) (2008) 1276–1283. doi:10.1002/mrm.21789.
[34] P. Pullens, A. Roebroeck, R. Goebel, Ground truth hardware phantoms for validation of diffusion-weighted MRI applications, Journal of Magnetic Resonance Imaging 32 (2) (2010) 482–488. doi:10.1002/jmri.22243.
[35] M. C. Tourell, S. K. Powell, K. I. Momot, Diffusion tensor of water in partially aligned fibre networks, Journal of Physics D: Applied Physics 46 (45) (2013). doi:10.1088/0022-3727/46/45/455401.
[36] W. Lee, H. Rahman, M. E. Kersh, K. C. Toussaint, Application of quantitative second-harmonic generation microscopy to posterior cruciate ligament for crimp analysis studies, Journal of Biomedical Optics 22 (4) (2017) 046009. doi:10.1117/1.jbo.22.4.046009.
[37] C. T. Thorpe, C. Klemt, G. P. Riley, H. L. Birch, P. D. Clegg, H. R. Screen, Helical sub-structures in energy-storing tendons provide a possible mechanism for efficient energy storage and return, Acta Biomaterialia 9 (8) (2013) 7948–7956. doi:10.1016/j.actbio.2013.05.004.
[38] B. E. Peterson, S. E. Szczesny, Dependence of tendon multiscale mechanics on sample gauge length is consistent with discontinuous collagen fibrils, Acta Biomaterialia 117 (2020) 302–309. doi:10.1016/j.actbio.2020.09.046.
[39] S. E. Szczesny, D. M. Elliott, Interfibrillar shear stress is the loading mechanism of collagen fibrils in tendon, Acta Biomaterialia 10 (6) (2014) 2582–2590. doi:10.1016/j.actbio.2014.01.032.

[40] J. W. Hearle, P. Grosberg, S. Backer, Structural Mechanics of Fibers, Yarns, and Fabrics, Wiley-Interscience, New York, 1969.
[41] S. P. Reese, S. A. Maas, J. A. Weiss, Micromechanical models of helical superstructures in ligament and tendon fibers predict large Poisson's ratios, Journal of Biomechanics 43 (7) (2010) 1394–1400. doi:10.1016/j.jbiomech.2010.01.004.
[42] C. V. Le, D. G. Phillips, The low-stress tensile behaviour of single worsted yarns, Journal of the Textile Institute 98 (5) (2007) 421–429. doi:10.1080/00405000701570856.
[43] R. A. Pineda Guzman, M. E. Kersh, Replication of the tensile behavior of knee ligaments using architected acrylic yarn, Journal of the Mechanical Behavior of Biomedical Materials 118 (December 2020) (2021) 104339. doi:10.1016/j.jmbbm.2021.104339.
[44] L. R. Arant, J. D. Roth, Development and evaluation of ligament phantoms targeted for shear wave tensiometry, Journal of the Mechanical Behavior of Biomedical Materials 126 (September 2021) (2021) 104984. doi:10.1016/j.jmbbm.2021.104984.
[45] G. G. Handsfield, L. C. Slane, H. R. Screen, Nomenclature of the tendon hierarchy: An overview of inconsistent terminology and a proposed size-based naming scheme with terminology for multi-muscle tendons, Journal of Biomechanics 49 (13) (2016) 3122–3124. doi:10.1016/j.jbiomech.2016.06.028.
[46] N. M. Naughton, C. G. Tennyson, J. G. Georgiadis, Lattice Boltzmann method for simulation of diffusion magnetic resonance imaging physics in multiphase tissue models, Physical Review E 102 (4) (2020) 043305. doi:10.1103/PhysRevE.102.043305.
[47] J. Veraart, E. Fieremans, D. S. Novikov, Diffusion MRI noise mapping using random matrix theory: Diffusion MRI Noise Mapping, Magnetic Resonance in Medicine 76 (5) (2016) 1582–1593. doi:10.1002/mrm.26059.
[48] J.-D. Tournier, R. Smith, D. Raffelt, R. Tabbara, T. Dhollander, M. Pietsch, D. Christiaens, B. Jeurissen, C.-H. Yeh, A. Connelly, MRtrix3: A fast, flexible and open software framework for medical image processing and visualisation, NeuroImage 202 (2019) 116137. doi:10.1016/j.neuroimage.2019.116137.
[49] B. M. Damon, Z. Ding, M. T. Hooijmans, A. W. Anderson, X. Zhou, C. L. Coolbaugh, M. K. George, B. A. Landman, A MATLAB toolbox for muscle diffusion-tensor MRI tractography, Journal of Biomechanics 124 (2021) 110540. doi:10.1016/j.jbiomech.2021.110540.
[50] G. M. Thornton, T. D. Schwab, T. R. Oxland, Cyclic loading causes faster rupture and strain rate than static loading in medial collateral ligament at high stress, Clinical Biomechanics 22 (8) (2007) 932–940. doi:10.1016/j.clinbiomech.2007.05.004.
[51] C. M. van Wyk, 20—Note on the compressibility of wool, Journal of the Textile Institute Transactions 37 (12) (1946) T285–T292. doi:10.1080/19447024608659279.
[52] H. A. Lynch, W. Johannessen, J. P. Wu, A. Jawa, D. M. Elliott, Effect of Fiber Orientation and Strain Rate on the Nonlinear Uniaxial Tensile Material Properties of Tendon, Journal of Biomechanical Engineering 125 (5) (2003) 726–731. doi:10.1115/1.1614819.
[53] R. Lorenz, M. E. Bellemann, J. Hennig, K. A. Il'Yasov, Anisotropic phantoms for quantitative diffusion tensor imaging and fiber-tracking validation, Applied Magnetic Resonance 33 (4) (2008) 419–429. doi:10.1007/s00723-008-0087-7.
[54] D. T. Fung, V. M. Wang, D. M. Laudier, J. H. Shine, J. Basta-Pljakic, K. J. Jepsen, M. B. Schaffler, E. L. Flatow, Subrupture tendon fatigue damage, Journal of Orthopaedic Research 27 (2) (2009) 264–273. doi:10.1002/jor.20722.
[55] B. R. Freedman, A. Zuskov, J. J. Sarver, M. R. Buckley, L. J. Soslowsky, Evaluating changes in tendon crimp with fatigue loading as an ex vivo structural assessment of tendon damage, Journal of Orthopaedic Research 33 (6) (2015) 904–910. doi:10.1002/jor.22875.
[56] A. Alia, G. Fantozzi, N. Godin, J. Adrien, H. Osmani, P. Reynaud, Multi-instrumented analysis of fatigue behavior and damage mechanisms in jute fiber-reinforced polyester composites, International Journal of Fatigue 167 (2023) 107306. doi:10.1016/j.ijfatigue.2022.107306.
[57] C. W. Imhauser, R. N. Kent, J. Boorman-Padgett, R. Thein, T. L. Wickiewicz, A. D. Pearle, New parameters describing how knee ligaments carry force in situ predict interspecimen variations in laxity during simulated clinical exams, Journal of Biomechanics 64 (2017) 212–218. doi:10.1016/j.jbiomech.2017.09.032.
[58] H. R. C. Screen, D. A. Lee, D. L. Bader, J. C. Shelton, An investigation into the effects of the hierarchical structure of tendon fascicles on micromechanical properties, Proceedings of the Institution of Mechanical Engineers , Part H : Journal of Engineering in Medicine 218 (2004) 109–119.
[59] E. M. Wojtys, M. L. Beaulieu, J. A. Ashton-Miller, New perspectives on ACL injury: On the role

of repetitive sub-maximal knee loading in causing ACL fatigue failure, Journal of Orthopaedic Research 34 (12) (2016) 2059–2068. doi:10.1002/jor.23441.